MULTISCALE MODEL. SIMUL.
Vol. 12, No. 4, pp. 1607–1621

NUMERICAL SIMULATIONS OF X-RAY FREE ELECTRON LASERS (XFEL)*

PAOLO ANTONELLI†, AGISSILAOS ATHANASSOULIS‡, ZHONGYI HUANG§, AND PETER A. MARKOWICH¶

Abstract. We study a nonlinear Schrödinger equation which arises as an effective single particle model in X-ray free electron lasers (XFEL). This equation appears as a first principles model for the beam-matter interactions that would take place in an XFEL molecular imaging experiment in [A. Fratalocchi and G. Ruocco, *Phys. Rev. Lett.*, 106 (2011), 105504]. Since XFEL are more powerful by several orders of magnitude than more conventional lasers, the systematic investigation of many of the standard assumptions and approximations has attracted increased attention. In this model the electrons move under a rapidly oscillating electromagnetic field, and the convergence of the problem to an effective time-averaged one is examined. We use an operator splitting pseudospectral method to investigate numerically the behavior of the model versus that of its time-averaged version in complex situations, namely the energy subcritical/mass supercritical case and in the presence of a periodic lattice. We find the time-averaged model to be an effective approximation, even close to blowup, for fast enough oscillations of the external field. This work extends previous analytical results for simpler cases [P. Antonelli, A. Athanassoulis, H. Hajaiej, and P. Markowich, *Arch. Ration. Mech. Anal.*, 211 (2014), pp. 711–732].

Key words. X-ray free electron laser, nonlinear Schrödinger equation, time-splitting spectral method, Bloch decomposition

AMS subject classifications. 65M70, 74Q10, 35B27, 81Q20

DOI. 10.1137/130927838

1. Introduction.

In this paper we study a first principles model for beam-matter interaction in X-ray free electron lasers (XFEL) [6, 7]. Recent developments using XFEL include the observation of the motion of atoms [3], measuring the dynamics of atomic vibrations [8], and biomolecular imaging [14]. The fundamental model for XFEL is the following nonlinear Schrödinger equation:

$$\begin{cases} i\hbar\partial_t\psi = \frac{1}{2m}(i\hbar\nabla - e\mathbf{A})^2\psi + Ze\frac{1}{|\mathbf{x}|}\psi + e^2(|\cdot|^{-1} * |\psi|^2)\psi - \lambda|\psi|^\sigma\psi, \\ \psi(t,\mathbf{x})|_{t=0} = \psi_0(\mathbf{x}), \end{cases} \tag{1.1}$$

on $\mathbb{R}^3$. Here m_e is the electron mass, e the electron charge, Z the atomic number, and $\hbar$ the scaled (by 2π) Planck constant. The constant $\lambda > 0$ measures the strength of the local attractive nonlinearity with power $\sigma > 0$, in particular $\sigma = \frac{2}{3}$ and $\lambda = 3e^2\left(\frac{3}{8\pi}\right)^{1/3}$ for the local Hartree–Fock approximation.

*Received by the editors July 5, 2013; accepted for publication (in revised form) August 5, 2014; published electronically November 4, 2014.
http://www.siam.org/journals/mms/12-4/92783.html

†Centro di Ricerca Matematica Ennio De Giorgi, Scuola Normale Superiore, Piazza dei Cavalieri, 3, 56100 Pisa, Italy (paolo.antonelli@sns.it).

‡Department of Mathematics, University of Leicester, 1 University Road, LE1 7RH Leicester, UK (aa816@le.ac.uk).

§Corresponding author. Department of Mathematical Sciences, Tsinghua University, Beijing 100084, China (zhuang@math.tsinghua.edu.cn). The research of this author was partially supported by NSFC Projects 11322113, 91330203, and by the National Basic Research Program of China under grant 2011CB309705.

¶MCSE Division, King Abdullah University of Science and Technology (KAUST), Thuwal 23955-6900, Saudi Arabia (P.Markowich@kaust.edu.sa). The research of this author was supported by the Royal Society through a Wolfson Research Merit Award, and by the Award KUK-I1-007-43, funded by KAUST.

A solution $\psi = \psi(t, \mathbf{x})$ of this Schrödinger equation can be considered as the wave function of an electron beam, interacting self-consistently through the repulsive Coulomb (Hartree) force, the attractive local Fock-type approximation with strength λ and exponent σ, and interacting repulsively with an atomic nucleus, located at the origin. The vector field $\mathbf{A} = \mathbf{A}(t)$ represents an external electromagnetic field, which we shall assume to depend on time t only (not on position $\mathbf{x}$).

In the experimental setup of interest [6, 7] the magnetic field is rapidly oscillating. This effect of oscillating external magnetic field appears often in the modeling of undulators; here the aim is to justify systematically the use of an effective time-averaged magnetic field, in the presence of beam-matter interaction.

In [1] it was shown that, under appropriate assumptions, the solution of (1.1) can be approximated, in the asymptotic regime $|\omega| \gg 1$, by the solution of an effective time-averaged Schrödinger initial value problem. The present work is a continuation of that line of investigation in more general contexts. More specifically, with the help of numerical simulations, we are able to tackle more detailed questions with respect to the role of the fast magnetic field, the mode of convergence, and attack problems with blowup. Moreover, we investigate the effect of a periodic lattice on the model.

1.1. The model. We scale (1.1) by choosing a characteristic time scale t_c and a characteristic spatial scale x_c. Defining the semiclassical parameter $\varepsilon = \frac{\hbar t_c}{2m_e x_c^2}$, we obtain after rescaling

$$i\varepsilon\partial_t\psi = (i\varepsilon\nabla - \mathbf{A})^2\psi + \frac{c}{|x|}\psi + C_1(|\cdot|^{-1} * |\psi|^2)\psi - a|\psi|^\sigma\psi,$$

where $c = eZ\frac{t_c^2}{2m_e x_c}$, $C_1 = e^2\frac{t_c^6}{8m_e^3 x_c^4}$, $a = \lambda\big(\frac{t_c^2}{2m_e x_c^2}\big)^{\sigma+1}$. Here also ψ and $\mathbf{A}$ were scaled appropriately.

A standard transform is used to simplify the original equation and bring it to a form more amenable to analysis as well as computation. By setting

$$u(t, \mathbf{x}) = \psi\left(t, \mathbf{x} + b(t)\right) \exp\left(\frac{i}{\varepsilon}\int_0^t |\mathbf{A}(s)|^2 ds\right), \tag{1.2}$$

where $b(t) = 2\int_0^t \mathbf{A}(s)ds$, one readily checks that u satisfies the initial value problem

$$\begin{cases} i\varepsilon\partial_t u = -\varepsilon^2\Delta u + \frac{c}{|\mathbf{x}-b(t)|}u + C_1(|\cdot|^{-1} * |u|^2)u - a|u|^\sigma u, \\ u^\omega(t, \mathbf{x})\big|_{t=0} = u_0(\mathbf{x}), \end{cases} \tag{1.3}$$

where $u_0 := \psi_0$. Now we choose the scales x_c, t_c such that $\varepsilon = 1$ (thus relating x_c and t_c by $2m_e x_c^2 = \hbar t_c$), since we are mostly interested in the fully quantum mechanical case, and we fix

$$b(t) = e(t)\sin(2\pi\omega t),$$

where $e : \mathbb{R} \to \mathbb{R}^3$ is a smooth vector field, slowly varying in time. We consider the high frequency case,

$$|\omega| \gg \frac{\text{sec}}{t_c} = \frac{\hbar}{2m_e}\left(\frac{\text{meter}}{x_c}\right)^2 \approx 5 \times 10^{-3}\left(\frac{\text{meter}}{x_c}\right)^2,$$

and study the asymptotic regime $|\omega| \to \infty$. In particular, we shall investigate the convergence of solutions of

$$\begin{cases} i\partial_t u^\omega = -\Delta u^\omega + V^\omega u^\omega + C_1(|\cdot|^{-1} * |u^\omega|^2)u^\omega - a|u^\omega|^\sigma u^\omega, \\ u^\omega(t, \mathbf{x})\big|_{t=0} = u_0(\mathbf{x}), \end{cases} \tag{1.4}$$

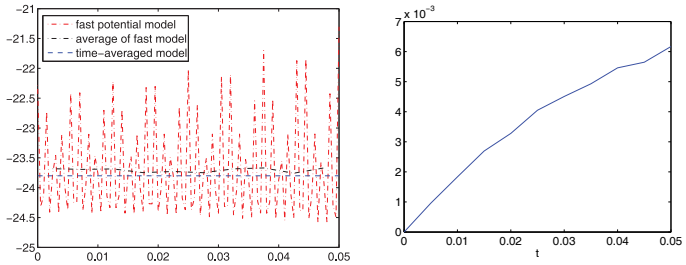

FIG. 1. *Convergence of the energy for problem* (1.4) *to that of* (1.6) *is a good way to keep track of the time-averaging, as well as a diagnostic tool for the computation. Here we show the differences of the energies (left) and the wave functions (right) between the fast potential model and the time-averaged model. We take the time local average of* $E^\omega(t)$ *over* $[t, t+0.005]$.

where the fast oscillatory potential is given by

$$V^\omega(t,x) := \frac{c}{|\mathbf{x} - e(t)\sin(2\pi\omega t)|}, \tag{1.5}$$

to solutions of the approximate problem (see [1] and Theorem 1 there)

$$\begin{cases} i\partial_t u = -\Delta u + \langle V\rangle u + C_1(|\cdot|^{-1} * |u|^2)u - a|u|^\sigma u, \\ u(t,\mathbf{x})\big|_{t=0} = u_0(\mathbf{x}), \end{cases} \tag{1.6}$$

with $\langle V\rangle$ the time-*averaged* potential given by

$$\langle V\rangle(t,\mathbf{x}) := \int_0^1 \frac{c}{|\mathbf{x} - e(t)\sin(2\pi s)|} ds. \tag{1.7}$$

We remark that (1.7) is well defined as the weak limit of V^ω defined in (1.5) in the space $L^\infty(\mathbb{R}; L^{3-}(\mathbb{R}^3) + L^{3+}(\mathbb{R}^3))$ as $|\omega| \to \infty$ (see [1] for more details). Passing back and forth between u and ψ (models (1.4) and (1.1)) is completely straightforward, by virtue of the transformation (1.2).

Remark 1.1. In molecular imaging (spatial characteristic scale of the order of magnitude of thousand nanometers, temporal characteristic scale of some femtoseconds), we compute $\omega \gg 10^{15}$. Therefore it makes sense to investigate the asymptotic regime. We shall demonstrate later on that this is reached already for much smaller values of ω.

1.2. Main objectives. The main result of [1] was the following.

THEOREM 1.1. *Let* $0 < \sigma < 4/3$, $u_0 \in L^2(\mathbb{R}^3)$. *Assume that* $u^\omega, u \in C(\mathbb{R}; L^2(\mathbb{R}^3))$ *are the unique global solutions of* (1.4), (1.6), *respectively. Then for each finite time* $0 < T < \infty$ *and for each admissible Strichartz index pair* (q,r) *we have*

$$\|u^\omega - u\|_{L^q([0,T];L^r(\mathbb{R}^3))} \to 0 \qquad \text{as } |\omega| \to \infty.$$

We use this averaging result as a benchmark (Example 3.1); the energy for the fast problem is observed to converge weakly to the energy for the averaged problem (and not strongly L^∞ in time; cf. Figure 1). We proceed to investigate mass supercritical problems in Example 3.2, i.e., the exponent σ is taken to be larger than $\frac{4}{3}$. The point is to investigate whether the time-averaged model still gives a good description near blowup. We proceed to an example that highlights the interaction with the (rapidly

oscillating) external electromagnetic potential in Example 3.3, and with a two-time scale–dependent electromagnetic potential in Example 3.4. Finally, we investigate the interaction with a periodic lattice in Example 3.5.

2. Numerical methods for nonlinear Schrödinger equations (1.4) and (1.6). As we have shown in [2, 9, 10, 11], the time-splitting pseudospectral/Bloch-decomposition-based pseudospectral methods work well for (non)linear Schrödinger equations (with periodic potential), and thus we shall focus on these two kinds of methods in this paper. We have shown that these two methods have spectral convergency in spatial discretization [2, 9, 10, 11].

2.1. Time-splitting spectral algorithm. We solve (1.4) or (1.6) by a classical time-splitting spectral scheme as follows [2, 11]:

Step 1. We solve the equation

$$\mathrm{i}\partial_t u_1 = -\Delta u_1, \tag{2.1}$$

on a fixed time interval Δt, relying on the *pseudospectral* method. Thus we can get the value of u_1 at new time t^{n+1} by

$$u_1^{n+1} = \left(e^{-\mathrm{i}\Delta t|\xi|^2}\hat{u}_1^n(\xi)\right)^\vee,$$

where "$\wedge$" and "$\vee$" denote the Fourier and inverse Fourier transforms, respectively.

Let $\rho(t^{n+1},\mathbf{x}) = |u_1(t^{n+1},\mathbf{x})|^2$; then we compute the Hartree potential $V_{Hartree}$ by

$$V_{Hartree}(t^{n+1},\mathbf{x}) = \left(\frac{1}{|\xi|^2}\hat{\rho}(t^{n+1},\xi)\right)^\vee.$$

Step 2. We solve the ordinary differential equation

$$\mathrm{i}\partial_t u_2 = \left(C_1 V_{Hartree} + V(t,\mathbf{x}) - a|u_2|^\sigma\right)u_2, \qquad u_2(t^n,\mathbf{x}) = u_1(t^{n+1},\mathbf{x}), \tag{2.2}$$

on the same time-interval; here $V(t,\mathbf{x})$ is given by (1.5) or (1.7). It is easy to check that in this step the density $\rho(t,\mathbf{x}) \equiv |u_2|^2(t,\mathbf{x})$ and consequently the Hartree potential do not change in time; hence

$$u_2(t+\Delta t,\mathbf{x}) = u_2(t,\mathbf{x})\,\exp\left(-\mathrm{i}\int_t^{t+\Delta t}\left(C_1 V_{Hartree}(\mathbf{x}) + V(s,\mathbf{x}) - a\rho^{\frac{\sigma}{2}}(\mathbf{x})\right)ds\right)$$

with $\rho(\mathbf{x}) = |u_1(t^{n+1},\mathbf{x})|^2$, $V_{Hartree}(x) = \left(\frac{1}{|\xi|^2}\hat{\rho}(\xi)\right)^\vee$.

The key is to calculate the oscillatory integral,

$$\int_t^{t+\Delta t}\frac{1}{|\mathbf{x}-b(s)|}ds \equiv \int_t^{t+\Delta t}\frac{1}{|\mathbf{x}-e(s)\sin(2\pi\omega s)|}ds, \tag{2.3}$$

where $|\omega| \gg 1$, particularly due to the occurrence of the singularity in the kernel. Therefore, we use a regularization technique. For example, we could take

$$\int_t^{t+\Delta t}\frac{1}{|\mathbf{x}-b(s)|}ds \approx \int_t^{t+\Delta t}\Phi^\eta\left(\frac{1}{|\mathbf{x}-b(s)|}\right)ds, \tag{2.4}$$

where

$$\Phi^\eta\left(\frac{1}{|\mathbf{x}-b(s)|}\right)=\left(\frac{2}{\eta}\right)^{\frac{3}{2}}\int_{\mathbb{R}^3}e^{-2\pi\frac{|\mathbf{x}-\mathbf{x}'|^2}{\eta}}\frac{1}{|\mathbf{x}'-b(s)|}d\mathbf{x}'.$$

In section 4 we will discuss stability with respect to perturbations of the potential. The energies for the two models are

$$E^\omega(t):=\int_{\mathbb{R}^3}\left(|\nabla u^\omega|^2+\frac{C_1}{2}|\nabla V^\omega_{Hartree}|^2+cV^\omega|u^\omega|^2-a\frac{2}{\sigma+2}|u^\omega|^{\sigma+2}\right)d\mathbf{x} \tag{2.5}$$

and

$$E(t):=\int_{\mathbb{R}^3}\left(|\nabla u|^2+\frac{C_1}{2}|\nabla V_{Hartree}|^2+c\langle V\rangle|u|^2-a\frac{2}{\sigma+2}|u|^{\sigma+2}\right)d\mathbf{x}, \tag{2.6}$$

respectively. The total mass,

$$M(t):=\int_{\mathbb{R}^3}|u(t,\mathbf{x})|^2d\mathbf{x}, \tag{2.7}$$

is conserved in both models.

2.2. Bloch-decomposition-based time-splitting spectral algorithm. If we consider an external potential $V_{ext}(\mathbf{x})$ in (1.1) [8, 13], we have

$$i\varepsilon\partial_t\psi=(i\varepsilon\nabla-A)^2\psi+V_{ext}(\mathbf{x})\psi+c\frac{1}{|\mathbf{x}|}\psi+C_1(|\cdot|^{-1}*|\psi|^2)\psi-a|\psi|^\sigma\psi.$$

By the same transformation (1.2) and by fixing $\varepsilon=1$, we obtain the equation

$$i\partial_t u^\omega=-\Delta u^\omega+V_{ext}\left(\mathbf{x}-b(t)\right)u^\omega+V^\omega u+C_1(|\cdot|^{-1}*|u^\omega|^2)u^\omega-a|u^\omega|^\sigma u^\omega, \tag{2.8}$$

and its time-averaged problem is

$$i\partial_t u=-\Delta u+\langle V_{ext}\rangle u+\langle V\rangle u+C_1(|\cdot|^{-1}*|u|^2)u-a|u|^\sigma u, \tag{2.9}$$

with

$$\langle V_{ext}\rangle(t,\mathbf{x})=\int_{-\frac{1}{2}}^{\frac{1}{2}}V_{ext}\left(\mathbf{x}-e(t)\sin(2\pi s)\right)ds.$$

In particular, if we consider a case with a periodic potential $V_\Gamma(\mathbf{x})$ [8, 13], i.e., when $V_\Gamma(\mathbf{y})$ is periodic w.r.t. to a regular lattice Γ,

$$V_\Gamma(\mathbf{y}+\gamma)=V_\Gamma(\mathbf{y})\quad\forall\gamma\in\Gamma,\mathbf{y}\in\mathbb{R}^3,$$

equations (2.8)–(2.9) become

$$i\partial_t u^\omega=-\Delta u^\omega+V_\Gamma\left(\mathbf{x}-b(t)\right)u^\omega+V^\omega u+C_1(|\cdot|^{-1}*|u^\omega|^2)u^\omega-a|u^\omega|^\sigma u^\omega, \tag{2.10}$$

and the corresponding time-averaged problem is

$$i\partial_t u=-\Delta u+\langle V_\Gamma\rangle(t,\mathbf{x})u+\langle V\rangle u+C_1(|\cdot|^{-1}*|u|^2)u-a|u|^\sigma u, \tag{2.11}$$

with

$$\langle V_\Gamma\rangle(t,\mathbf{x}) = \int_{-\frac{1}{2}}^{\frac{1}{2}} V_\Gamma\left(\mathbf{x} - e(t)\sin(2\pi s)\right) ds.$$

We solve (2.10) or (2.11) by using the *Bloch-decomposition-based time-splitting method*; see [9, 10].

Step 1. We solve the equation

$$\mathrm{i}\partial_t u_1 = -\Delta u_1 + V_\Gamma(t,\mathbf{x})\, u_1, \tag{2.12}$$

on a fixed time interval Δt, relying on the *Bloch-decomposition-based pseudospectral* method.

Let $\rho(t^{n+1},\mathbf{x}) = |u_1(t^{n+1},\mathbf{x})|^2$; then we obtain the Hartree potential $V_{Hartree}$ by

$$V_{Hartree}\left(t^{n+1},\mathbf{x}\right) = \left(\frac{1}{|\xi|^2}\hat{\rho}(t^{n+1},\xi)\right)^\vee.$$

Step 2. Then, we solve the ordinary differential equation

$$\mathrm{i}\partial_t u_2 = \left(C_1 V_{Hartree} + V(t,\mathbf{x}) - a|u_2|^\sigma\right) u_2, \qquad u_2\left(t^n,\mathbf{x}\right) = u_1\left(t^{n+1},\mathbf{x}\right), \tag{2.13}$$

on the same time-interval; here $V(t,\mathbf{x})$ is given by (1.5) or (1.7). It is easy to check that in this step the density $\rho(t,\mathbf{x}) \equiv |u_2|^2(t,\mathbf{x})$ and consequently the Hartree potential do not change in time; hence

$$u_2(t+\Delta t,\mathbf{x}) = u_2(t,\mathbf{x})\, \exp\left(-\mathrm{i}\int_t^{t+\Delta t}\left(C_1 V_{Hartree}(\mathbf{x}) + V(s,\mathbf{x}) - a\rho^{\frac{\sigma}{2}}(\mathbf{x})\right) ds\right),$$

with $\rho(\mathbf{x}) = \left|u_1(t^{n+1},\mathbf{x})\right|^2$, $V_{Hartree}(x) = \left(\frac{1}{|\xi|^2}\hat{\rho}(\xi)\right)^\vee$.

Remark 2.1. Certainly, if there is no lattice potential V_Γ, the above two algorithms give identical results. But we must include the lattice potential V_Γ when the interaction with laser or other lattice potential is not eligible. We will see that the Bloch-decomposition-based method is much more efficient in the case with lattice potential V_Γ than the traditional pseudospectral method (cf. Figures 16–17 below); i.e., we could use much more larger mesh sizes than with the traditional pseudospectral method to get the same accuracy.

3. Numerical implementation.

3.1. Convergence to the time-averaged model.

Example 3.1. Here we set the semiclassical parameter $\varepsilon = 1$, $e(t) = (0,0,1)^T$, $\sigma = \frac{2}{3}$, $a = 50$, $C_1 = 20$, $c = 1$. We compare the time-averaged model with the fast-potential model for different values of ω. We choose appropriate constants C_1 and c to make the two potential components in the energy comparable. See Table 1.

Remark 3.1. From Figures 2–5, we can see that as $|\omega| \to \infty$, the average of the energy $E^\omega(t)$ converges to the energy $E(t)$ of time-averaged model. The corresponding wave-function $u^\omega(t,\mathbf{x})$ also converges to $u(t,\mathbf{x})$ at least in the L^2-norm. Figure 4 also shows the conservation of $E(t)$ and $M(t)$.

TABLE 1
Example 3.1: *Errors between two models vs. frequency* ω.

ω	5	10	20	40
$\|u-u^\omega\|_{L^2}$	1.1E-1	5.4E-2	2.9E-2	1.8E-2
Convergence rate		1.0	0.9	0.7
$\|E-E^\omega\|_{L^1}$	7.1E-1	4.5E-1	2.9E-1	1.9E-1
Convergence rate		0.6	0.6	0.6

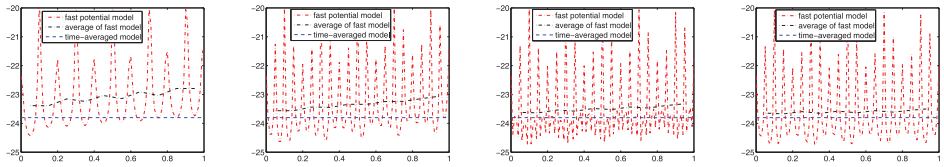

$\omega = 5$ $\omega = 10$ $\omega = 20$ $\omega = 40$

FIG. 2. *Example* 3.1: *Comparison of the energies of two models with different* ω. *Here we take the average of* $E^\omega(t)$ *over* $[t, t+0.1]$.

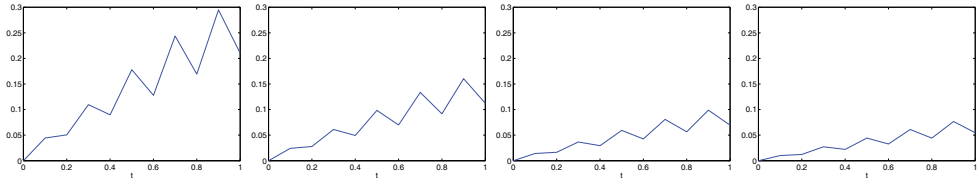

$\omega = 5$ $\omega = 10$ $\omega = 20$ $\omega = 40$

FIG. 3. *Example* 3.1: *The relative distance between the wave-functions of two models with different* ω: $\frac{\|u^\omega - u\|_{L^2}}{\|u\|_{L^2}}$.

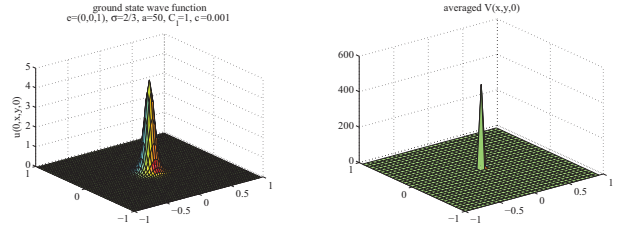

Initial datum $u_0(x, y, 0)$. $\overline{V}(x, y, 0)$.

FIG. 4. *Example* 3.1: *Graphs of the time-averaged model, with parameters* $\varepsilon = 1$, $e(t) = (0, 0, 1)^T$, $\sigma = \frac{2}{3}$, $a = 50$, $C_1 = 1$, $c = 0.001$. *Our numerical results show the conservation of the energy* $E(t)$ *(given by* (2.6)*) and mass* $M(t)$ *(given by* (2.7)*) in both the time-averaged model and the fast-potential model.*

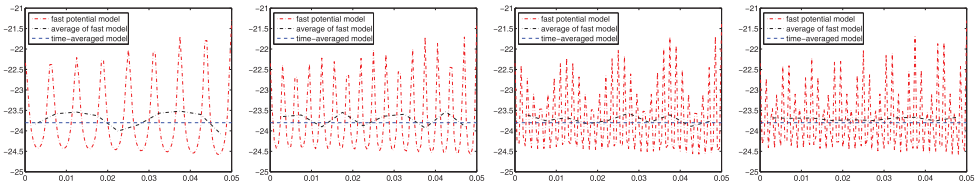

$\omega = 80$ $\omega = 160$ $\omega = 320$ $\omega = 640$

FIG. 5. *Example* 3.1: *The distance between the energies of two models with larger* ω *vs. time. Here we take the average of* $E^\omega(t)$ *over* $[t, t+0.005]$.

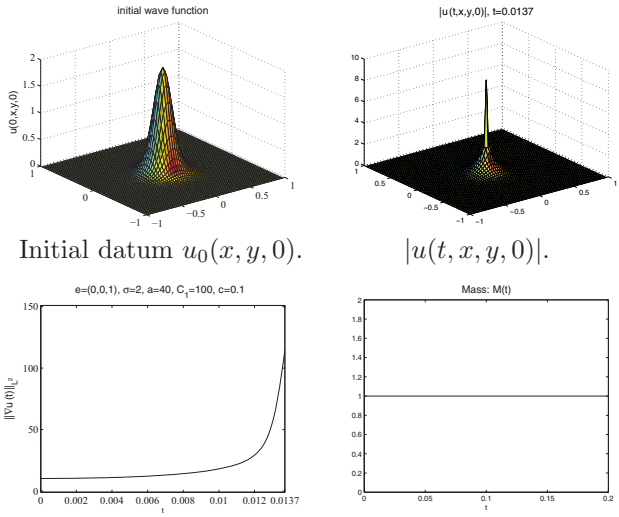

Initial datum $u_0(x, y, 0)$. $|u(t, x, y, 0)|$.

$\|\nabla u\|_{L^2}$ (given by (3.1)). $M(t)$ (given by (2.7)).

FIG. 6. *Example* 3.2: *Graphs of the time-averaged model, with parameters* $\varepsilon = 1$, $e(t) = (0, 0, 1)^T$, $\sigma = 2$, $a = 50$, $C_1 = 100$, $c = 0.1$. *Blowup case.*

3.2. Blowup tests.

Example 3.2. Here we consider an example with $\varepsilon = 1$, $e(t) = (0, 0, 1)^T$, $a = 50$, $C_1 = 100$, $c = 0.1$. We start the time-averaged model from a ground state for $\sigma = 2/3$ (cf. plot (a) in Figure 6). Then we consider (1.4) with a mass supercritical power-type nonlinearity, i.e., $\sigma > 4/3$, and we analyze the blowup of the norm

$$\|\nabla u\|_{L^2} = \left(\int_{\mathbb{R}^3} |\nabla u(t, \mathbf{x})|^2 d\mathbf{x} \right)^{1/2}. \tag{3.1}$$

In Figures 6–7, we can see that the blowup time decreases as σ increases.

Comparing the L^2-norms of the gradient of the wave-function for the time averaged model and the fast model in the blowup test, we can see that they are very similar in the super-critical case (cf. Figures 8–9 and Figures 6–7). They exhibit more differences in the subcritical case (see Figures 10–11).

Furthermore, from Figures 12–13, we can see that the Coulomb potential significantly impacts the wave packet at the early stage. This becomes particularly clear with slower blowup and smaller frequency ω.

3.3. Interaction of the magnetic field with the particle.

Example 3.3. Here we are interested in the patterns of interaction of the magnetic field with the particle, especially when a particle is shot towards the field and scattered by it. We set $e = (0, 0, 1)^T$ in (1.5), and choose an initial datum of the form

$$u_0(\mathbf{x}) = e^{-4|\mathbf{x}-(1,1,0)^T|^2 + i(x_1 - x_2)} \quad \text{for } \mathbf{x} = (x_1, x_2, x_3)^T.$$

In this example, we add a harmonic trap potential,

$$V(\mathbf{x}) = 50|\mathbf{x}|^2;$$

i.e., (1.4) becomes

$$i\partial_t u^\omega = -\Delta u^\omega + V\left(\mathbf{x} - b(t)\right) u^\omega + V^\omega u^\omega + C_1(|\cdot| * |u^\omega|^2)u^\omega - a|u^\omega|^\sigma u^\omega. \tag{3.2}$$

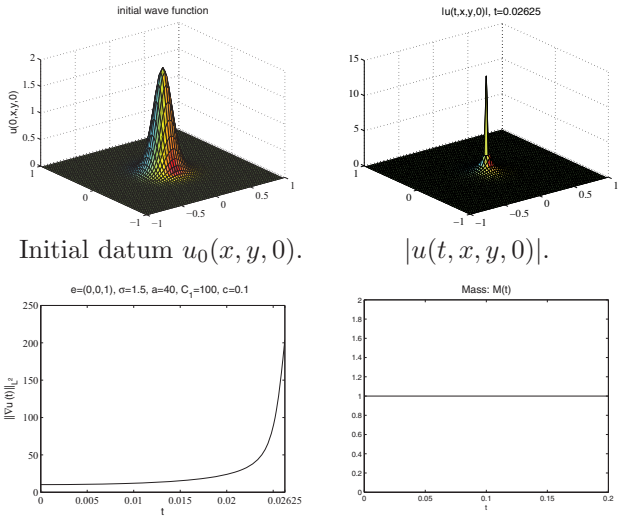

Initial datum $u_0(x, y, 0)$. $|u(t, x, y, 0)|$.

$\|\nabla u\|_{L^2}$ (given by (3.1)). $M(t)$ (given by (2.7)).

FIG. 7. *Example* 3.2: *Graphs of the time-averaged model, with parameters* $\varepsilon = 1$, $e(t) = (0, 0, 1)^T$, $\sigma = 1.5$, $a = 50$, $C_1 = 100$, $c = 0.1$. *Blowup case.*

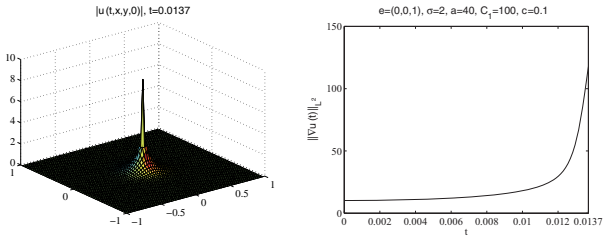

$u(t, x, y, 0)$. $\|\nabla u\|_{L^2}$ (given by (3.1)).

FIG. 8. *Example* 3.2: *Graphs of the fast-potential model, with parameters* $\varepsilon = 1$, $e(t) = (0, 0, 1)^T$, $\sigma = 2$, $a = 50$, $C_1 = 100$, $c = 0.1$, $\omega = 10^4$. *Blowup case.*

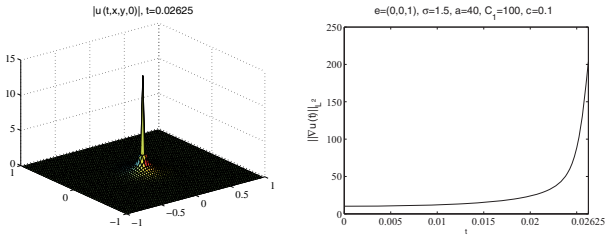

$u(t, x, y, 0)$. $\|\nabla u\|_{L^2}$ (given by (3.1)).

FIG. 9. *Example* 3.2: *Graphs of the fast-potential model, with parameters* $\varepsilon = 1$, $e(t) = (0, 0, 1)^T$, $\sigma = 1.5$, $a = 50$, $C_1 = 100$, $c = 0.1$, $\omega = 10^4$.

The results are shown in Figure 14. We can see that the wave packet moves under the interaction with the trap $V(\mathbf{x})$.

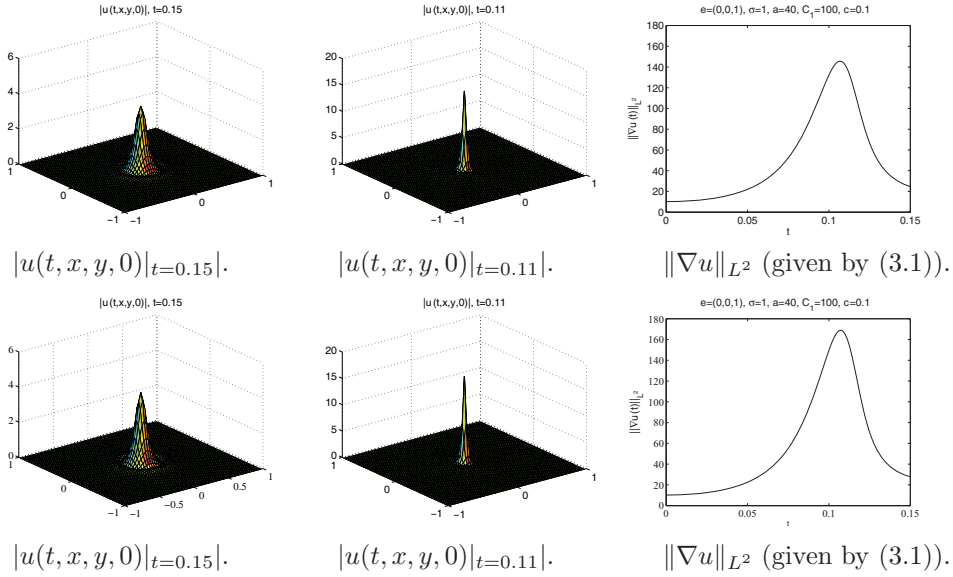

$|u(t,x,y,0)|_{t=0.15}|$. $|u(t,x,y,0)|_{t=0.11}|$. $\|\nabla u\|_{L^2}$ (given by (3.1)).

$|u(t,x,y,0)|_{t=0.15}|$. $|u(t,x,y,0)|_{t=0.11}|$. $\|\nabla u\|_{L^2}$ (given by (3.1)).

FIG. 10. *Example* 3.2: *Graphs of the fast-potential model (top graph) and time-averaged model (bottom graph), with parameters* $\varepsilon = 1$, $e(t) = (0,0,1)^T$, $\sigma = 1$, $a = 50$, $C_1 = 100$, $c = 0.1$, $\omega = 10^4$.

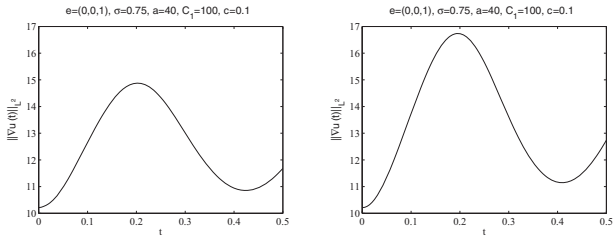

$\|\nabla u^\omega\|_{L^2}$ (given by (3.1)). $\|\nabla u\|_{L^2}$ (given by (3.1)).

FIG. 11. *Example* 3.2: *Graphs of the fast-potential model (left) and time-averaged model (right), with parameters* $\varepsilon = 1$, $e(t) = (0,0,1)^T$, $\sigma = 0.75$, $a = 50$, $C_1 = 100$, $c = 0.1$, $\omega = 10^4$.

3.4. Time-dependent vectors $e(t)$.

Example 3.4. We consider a time-dependent vector $e(t) = (-1,-1,-1)\sin 2\pi t$ in (1.5), and an initial datum of the form

$$u_0(x) = e^{-4|\mathbf{x}|^2}.$$

The results are shown in Figure 15. As $e(t)$ is slowly varying in time, its effects are not very pronounced except when $e(t)$ is close to 0.

3.5. Interaction with periodic lattice.

Example 3.5. Finally, we consider a case with periodic lattice, i.e., (1.4) becomes

$$i\partial_t u^\omega = -\Delta u^\omega + V^\omega u^\omega + V_\Gamma\left(\mathbf{x} - b(t)\right) u^\omega + C_1(|\cdot|^{-1} * |u^\omega|^2)u^\omega - a|u^\omega|^\sigma u^\omega, \tag{3.3}$$

and its time-averaged problem is

$$i\partial_t u = -\Delta u + \langle V\rangle u + \langle V_\Gamma\rangle u + C_1(|\cdot|^{-1} * |u|^2)u - a|u|^\sigma u. \tag{3.4}$$

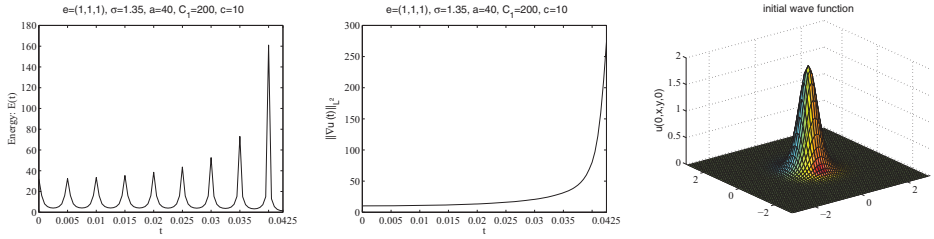

$E(t)$ (given by (2.5)). $\|\nabla u\|_{L^2}$ (given by (3.1)). $|u(t,x,y,0)|_{t=0}|$.

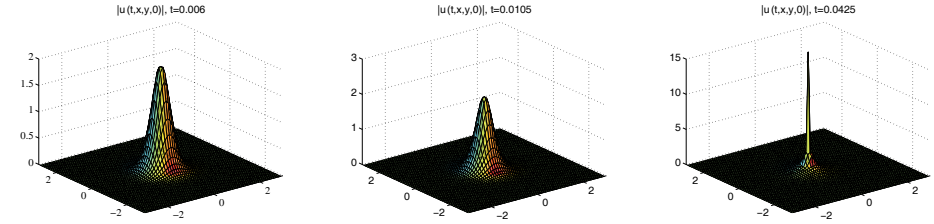

$|u(t,x,y,0)|_{t=0.006}|$. $|u(t,x,y,0)|_{t=0.0105}|$. $|u(t,x,y,0)|_{t=0.0425}|$.

FIG. 12. *Example* 3.2: *Graphs of the fast-potential model, with parameters* $\varepsilon = 1$, $e(t) = (1,1,1)^T$, $\sigma = 1.35$, $a = 40$, $C_1 = 200$, $c = 10$, $\omega = 10^2$.

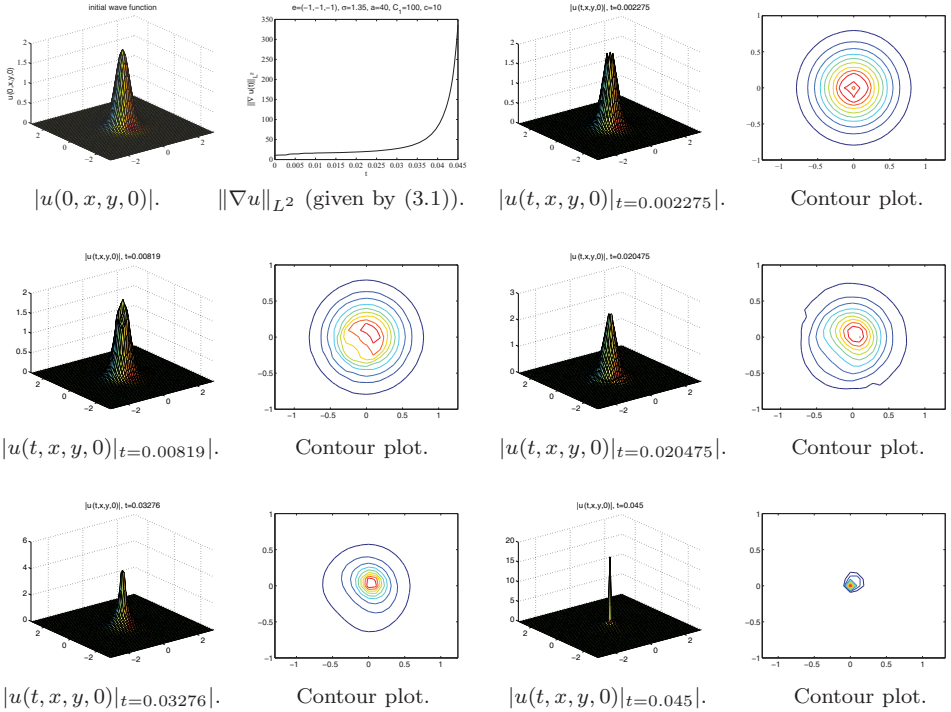

$|u(0,x,y,0)|$. $\|\nabla u\|_{L^2}$ (given by (3.1)). $|u(t,x,y,0)|_{t=0.002275}|$. Contour plot.

$|u(t,x,y,0)|_{t=0.00819}|$. Contour plot. $|u(t,x,y,0)|_{t=0.020475}|$. Contour plot.

$|u(t,x,y,0)|_{t=0.03276}|$. Contour plot. $|u(t,x,y,0)|_{t=0.045}|$. Contour plot.

FIG. 13. *Example* 3.2: *Graphs of the fast-potential model, with parameters* $\varepsilon = 1$, $e(t) = (-1,-1,-1)^T$, $\sigma = 1.35$, $a = 40$, $C_1 = 200$, $c = 10$, $\omega = 5$.

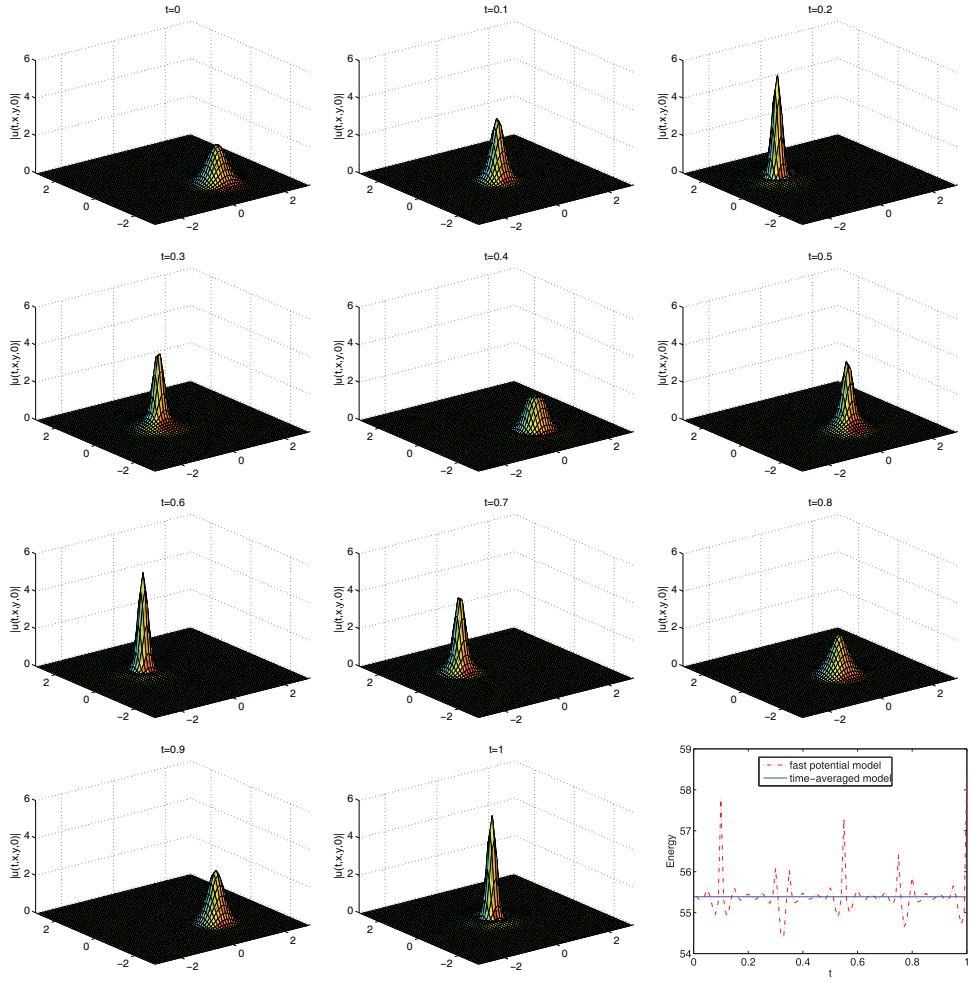

FIG. 14. *Example* 3.3: *Fast-potential model, with parameters* $\varepsilon = 1$, $e(t) = (0,0,1)^T$, $\sigma = \frac{2}{3}$, $a = 50$, $C_1 = 20$, $c = 1$, $\omega = 10^2$.

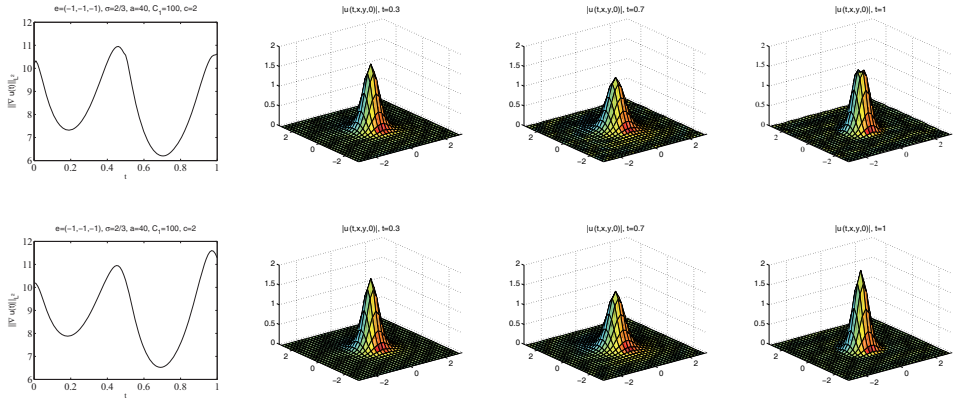

FIG. 15. *Example* 3.4: *Graphs of Example* 3.4 *for the fast-potential model (top graph) and the time-averaged model (bottom graph), with parameters* $\varepsilon = 1$, $e(t) = (-1,-1,-1)^T \sin 2\pi t$, $\sigma = \frac{2}{3}$, $a = 40$, $C_1 = 100$, $c = 2$, $\omega = 10^2$.

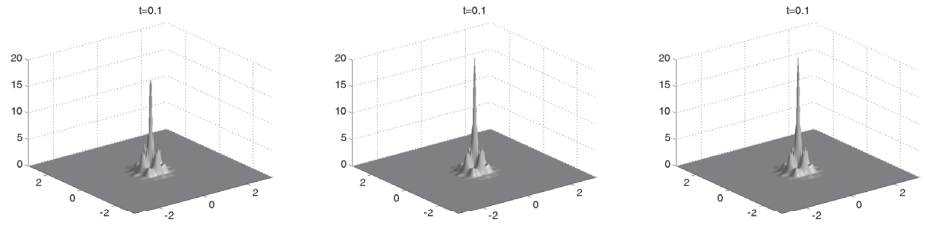

FIG. 16. *Graphs of* $|u^\omega(t,x,y,0)|^2$ *and* $|u(t,x,y,0)|^2$ *of Example* 3.5 *for the fast-potential model (left* $\omega = 80$*, middle* $\omega = 160$*) and time-averaged model (right) by our Bloch-decomposition-based algorithm given in section* 2.2*. The parameters are* $\varepsilon = \frac{1}{8}$*,* $e(t) = (0,0,1)^T$*,* $\sigma = \frac{2}{3}$*,* $a = 1$*,* $C_1 = 1$*,* $c = 2$*, mesh size* $h = \frac{1}{128}$*.*

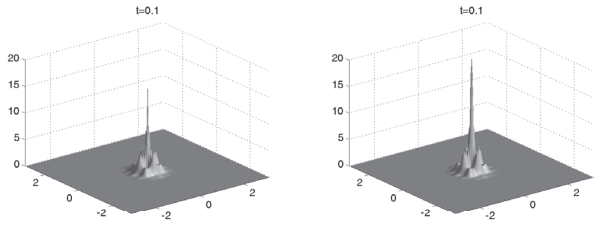

FIG. 17. *Graphs of* $|u(t,x,y,0)|^2$ *of Example* 3.5 *for the fast-potential model by the typical pseudospectral method given in section* 2.1*, with* $\omega = 160$ *and mesh size* $h = \frac{1}{128}$ *(left),* $h = \frac{1}{1024}$ *(right).*

We also take the initial datum of the form

$$u_0(x) = e^{-4|\mathbf{x}|^2}.$$

Here $V_\Gamma(\mathbf{y})$ is periodic w.r.t. to a regular lattice Γ,

$$V_\Gamma(\mathbf{y}+\gamma) = V_\Gamma(\mathbf{y}) \quad \forall \gamma \in \Gamma,\ \mathbf{y} \in \mathbb{R}^3.$$

For sake of simplicity, we choose

$$V_\Gamma(\mathbf{y}) = \sum_{l=1}^{3} \sin^2(\omega_l y_l) \quad \text{for } \mathbf{y} = (y_1, y_2, y_3)^T \in \mathbb{R}^3,$$

with $\omega_1 = \omega_2 = \omega_3 = 2\pi$.

The results are shown in Figures 16–17. We can see the interaction between the lattice potential and the wave packet. Certainly, the wave function of the fast model is more peaked than the solution of the time-averaged model. From these figures, we can also find that the Bloch-decomposition-based algorithm is more efficient than the traditional pseudospectral method in this case.

4. Stability estimate. In this section we present the analytical results needed in order to rigorously justify the approximation used in section 2. Because of the singularities of the Coulomb potential, we use a mollified version in the numerical simulation. Here we discuss the additional errors introduced by the smoothing.

In order to avoid technicalities we only state a proposition which shows that (1.4) is stable under perturbations of the potential. The proof is indeed quite standard, as

similar results are well known in the literature; see below for references. The proof of stability of (1.4) with respect to perturbations of the potential is done by adapting in a straightforward way the local well-posedness result. For further details we refer the reader to [12, 5] and [4, section 4].

THEOREM 4.1. *Let $V, \tilde{V}$ be two potentials such that $V, \tilde{V} \in L^\infty(\mathbb{R}; L^{\frac{3}{1+3\delta}}(\mathbb{R}^3) + L^{\frac{3}{1-3\delta}}(\mathbb{R}^3))$, $\nabla V, \nabla\tilde{V} \in L^\infty(\mathbb{R}; L^{\frac{3}{2+3\delta}}(\mathbb{R}^3) + L^{\frac{3}{2-3\delta}}(\mathbb{R}^3))$, for some $\delta > 0$ small. Let $u, \tilde{u}$ be the solutions of the Cauchy problems*

$$\begin{cases} i\partial_t u = -\Delta u + Vu + C_1(|\cdot|^{-1} * |u|^2)u - a|u|^\sigma u, \\ u(t,\mathbf{x})\big|_{t=0} = u_0(\mathbf{x}), \end{cases}$$

with the potential V and respectively with V replaced by $\tilde{V}$, and initial data u_0 and respectively $\tilde{u}_0 \in H^1(\mathbb{R}^3)$. Let $0 < T < \min\{T_{max}, \tilde{T}_{max}\}$, where $T_{max}, \tilde{T}_{max}$ are the maximal existence times for $u, \tilde{u}$, respectively. Then, for any admissible pair (q, r), we have

$$\begin{aligned} &\|u - \tilde{u}\|_{L^q((0,T);W^{1,r}(\mathbb{R}^3))} \\ &\le C\left(\|u_0 - \tilde{u}_0\|_{H^1} + \|V - \tilde{V}\|_{L_t^\infty(L_x^{\frac{3}{1+3\delta}} + L_x^{\frac{3}{1-3\delta}})} + \|\nabla(V - \tilde{V})\|_{L_t^\infty(L_x^{\frac{3}{2+3\delta}} + L_x^{\frac{3}{2-3\delta}})}\right). \end{aligned} \tag{4.1}$$

5. Conclusion. In this paper, we have proposed the time-splitting (Bloch-decomposition-based) pseudospectral method for simulating the XFEL Schrödinger equation (with and without periodic potential). Our simulation results go far beyond known analytical results [1]. In particular we have demonstrated numerically that the time-averaging procedure works in mass supercritical/energy subcritical cases, even up to blowup time. Moreover, we have shown numerically that the energy of the oscillatory problem converges weakly in time to the energy of the time-averaged problem (which is constant when the vector $e(t)$ is not dependent on time). Also, we have demonstrated the impact of external trapping potentials and periodic lattice potentials on the electron beam wave function, and numerically verified the time-averaged procedure in those cases.

REFERENCES

[1] P. ANTONELLI, A. ATHANASSOULIS, H. HAJAIEJ, AND P. MARKOWICH, *On the XFEL Schrödinger equation: Highly oscillatory magnetic potentials and time averaging*, Arch. Ration. Mech. Anal., 211 (2014), pp. 711–732.

[2] W. Z. BAO, S. JIN, AND P. MARKOWICH, *On time-splitting spectral approximations for the Schrödinger equation in the semiclassical regime*, J. Comput. Phys., 175 (2002), pp. 487–524.

[3] J. D. BROCK, *Watching atoms move*, Science, 315 (2007), pp. 609–610.

[4] T. CAZENAVE, *Semilinear Schrödinger Equations*, Courant Lect. Notes Math. 10, New York University, Courant Institute of Mathematical Sciences, New York, 2003.

[5] T. CAZENAVE AND M. SCIALOM, *A Schrödinger equation with time-oscillating nonlinearity*, Rev. Mat. Complut., 23 (2010), pp. 321–339.

[6] H. N. CHAPMAN, S. P. HAU-RIEGE, M. J. BOGAN, S. BAJT, A. BARTY, S. BOUTET, S. MARCHESINI, M. FRANK, B. W. WOODS, W. H. BENNER, R. A. LONDON, U. ROHNER, A. SZOKE, E. SPILLER, T. MOLLER, C. BOSTEDT, D. A. SHAPIRO, M. KUHLMANN, R. TREUSCH, E. PLONJES, F. BURMEISTER, M. BERGH, C. CALEMAN, G. HULDT, M. M. SEIBERT, AND J. HAJDU, *Femtosecond time-delay X-ray holography*, Nature, 448 (2007), pp. 676–679.

[7] A. FRATALOCCHI AND G. RUOCCO, *Single-molecule imaging with x-ray free electron lasers: Dream or reality?*, Phys. Rev. Lett., 106 (2011), 105504.

[8] D. M. Fritz, D. A. Reis, B. Adams, R. A. Akre, J. Arthur, C. Blome, P. H. Bucksbaum, A. L. Cavelieri, S. Engemann, S. Fahy, R. W. Falcone, P. H. Fuoss, K. J. Gaffney, M. J. George, J. Hajdu, M. P. Hertlein, P. B. Hillyard, M. Horn-von Hoegen, M. Kammler, J. Kaspar, R. Keinberger, P. Krejcik, S. H. Lee, A. M. Lindenberg, B. McFarland, D. Meyer, T. Montagne, É. D. Murray, A. J. Nelson, M. Nicoul, R. Pahl, J. Rudati, H. Schlarb, D. P. Siddons, K. Sokolowski-Tinten, Th. Tschentscher, D. von der Linde, and J. B. Hastings, *Ultrafast bond softening in bismuth: Mapping a solid's interatomic potential with X-rays*, Science, 315 (2007), pp. 633–636.

[9] Z. Huang, S. Jin, P. A. Markowich, and C. Sparber, *A Bloch decomposition–based split-step pseudospectral method for quantum dynamics with periodic potentials*, SIAM J. Sci. Comput., 29 (2007), pp. 515–538.

[10] Z. Huang, S. Jin, P. A. Markowich, and C. Sparber, *Numerical simulation of the nonlinear Schrödinger equation with multidimensional periodic potentials*, Multiscale Model. Simul., 7 (2008), pp. 539–564.

[11] Z. Huang, S. Jin, P. Markowich, C. Sparber, and C. Zheng, *A time-splitting spectral scheme for the Maxwell-Dirac system*, J. Comput. Phys., 208 (2005), pp. 761–789.

[12] T. Kato, *On nonlinear Schrödinger equations*, Ann. Inst. H. Poincaré, 46 (1987), pp. 113–129.

[13] B. W. J. McNeil and N. R. Thompson, *X-ray free-electron lasers*, Nature Photonics, 4 (2010), pp. 814–821.

[14] R. Neutze, R. Wouts, D. van der Spoel, E. Weckert, and J. Hajdu, *Potential for biomolecular imaging with femtosecond X-ray pulses*, Nature, 406 (2000), pp. 752–757.